RSC Advances

ROYAL SOCIETY OF CHEMISTRY

www.rsc.org/advances

Cite this: DOI: 10.1039/c0xx00000x

www.rsc.org/xxxxxx

ARTICLE TYPE

Edge-carboxylated graphene anchoring magnetite-hydroxyapatite nanocomposite for efficient 4-nitrophenol sensor†

G.Bharath[a], VediappanVeeramani[b], Shen-Ming Chen[b], Rajesh Madhu[b], M. Manivel Raja[c], A.Balamurugan[a], D. Mangalaraj[a], C. Viswanathan[a], N. Ponpandian*[,a]

Received (in XXX, XXX) XthXXXXXXXXX 20XX, Accepted Xth XXXXXXXXX 20XX
DOI: 10.1039/b000000x

Abstract

The surface chemistry and physical properties of edge-carboxylated graphene (ECG) has so far over sighted to understand the real world practical applications. The accurate identification of each possible oxygenated group on the surface of basal plane as well as the edges of ECG is necessary to understand the properties for their potential multifunctional applications. Herein, we report a simple high energy ball mill to prepare a large scale production of ECG from natural graphite flakes through interaction with aspartic acid under solid conditions. These 2 dimensional ECG sheets were anchored with the magnetite-hydroxyapatite (m-HAp) using a simple hydrothermal process.The prepared materials was systematically investigated by various analytical techniques to realize the structural, morphological, compositional and functional properties. These m-HAp dispersed ECG sheets can be further used to modify the glassy carbon electrode (GCE) for the sensitive and selective detection of 4-nitrophenol (4-NP) by cyclic voltammogram (CV) and differential pulsed voltammetry (DPV). The high specific surface area of 130 m^2g^{-1} for the m-HAp on ECG displays an excellent catalytic activity with reversible redox behavior of 4-NP. The modified electrode possesses a good detection limit and high sensitivity of 0.27 μM and 0.587 μA $\mu M^{-1}cm^{-2}$ towards 4-NP sensor, rendering practical industrial applications.

1. INTRODUCTION

Graphene is a rapidly rising unique two dimensional carbon material with outstanding indispensable properties such as electronic, high charge carrier mobility, optically transparent, high tensile strength, good thermal conductivity, an excellent theoretical surface area and mechanical properties. These functional properties will permit a wide range of applications like medicine, microelectronics, sensors, batteries *etc*.[1,2] All these qualities stimulate the researchers to prepare graphene by simple methods for the probable multifunctional applications. However, the large scale production of graphene is still a challenging task for the researchers. Thereby, the researchers focus on new synthetic strategies to make high quality graphene with large scale production in a cost effective manner. Several important methods have been already designated for the preparation of graphene, such as chemical vapor deposition (CVD), epitaxial growth on SiC, scotch tape, mechanochemical cleavage, chemical exfoliation, unzipping of carbon nanotubes and other organic synthetic protocols.[3-8] The commonly affordable chemical vapor deposition (CVD) method can produce high quality graphene with minor defects that can be used for highly demanding electronics and sensing applications. The Hummers and modified Hummers methods have been adopted to prepare bulk production of graphene oxide and graphene sheets. However, these methods exploited strong hazardous oxidizing agents and complicated multi-step process.[9,10] The reduction of graphene oxide requires reducing agents of hazardous hydrazine hydrate and sodium borohydride ($NaBH_4$). Moreover, the reduced graphene oxide in this method has structural defects induced at the basal planes and edges of the graphene sheets.

Recently, many researchers were produced the graphene with less structural defects by novel and simple methods. The mechanochemical is one those methods established for the fabrication of multi and few layers of graphene sheets with simple preparation, bulk production and cost effective.[11] This mechanochemical process will permit to introduce various functional groups at the edges of graphite. The high speed of the planetary rotation and the collision of stainless steel vials and balls generate sufficient kinetic energy for bond cleavages for the C-C aromatic graphite structure. The reactive carbon species such as oxalic acid, dry ice, melamine, triazine, potassium hydroxide, carbon dioxide- sulfur trioxide mixture, N,N dimethylformamide (DMF) and sodium dodecyl sulphate (SDS) are selective functionalized edges of cracked graphite.[11-16] The oxygen containing groups is possibly involved in the formation of nanoparticles anchored on the surface of negatively charged functionalized graphene. Nowadays graphene and their nanocomposites shows excellent electrochemical behavior. The graphene/metal oxides, graphene/conducting polymers and graphene/hydroxyapatite/Nafion nanocomposite are

systematically explored for electrochemical biosensors and it uses to determine the H_2O_2, Glucose, dopamine, ascorbic acid and uric acid *etc*.[15-21] Morever graphene based nanocomposite materials are widely used for the determination of toxic organic and inorganic compounds in contaminated water by various analytical techniques.[22-24]

Graphene/graphene based nanocomposites and hydroxyapatite provides enormous impact on the detection of toxic/polluted compounds for environmental remediation. Especially, graphene oxide, β-cyclodextrin functionalized graphene, N-doped graphene and molecularly imprinted polymer based graphene nanocomposite, hydroxyapatite, Fe_3O_4 incorporated HAp or HAp/Fe_3O_4nanocomposites are important functional nanomaterials for excellent detection of phenols-based aromatic nitro compounds in various contaminated environmental water samples by electrochemical detections.[22-29] It is important to detect the aromatic nitro compounds which are commonly produced from pharmaceuticals, pesticides, dyes and chemical industries which are toxic to the human body, animals, plants and aquatic life. In particular, 4-Nitrophenol (4-NP) is a toxic derivative cited in the list of priority pollutants by the U.S.A Environmental Production Agency (EPA). The 4-NP has been found not only in industrial waste water but also lake and sea water. The United States EPA will permit the allowed limit of 4-NP in drinking water as 0.43 μM. Therefore, the determination of highly toxic 4-NP is important and essential. It requires a simple and reliable method for the determination of 4-NP in environmental water samples. Several electrochemical and spectroscopic techniques such as cyclic voltammetry (CV), differential pulsed voltammetry (DPV), fluorescence, high-performance liquid chromatography and spectrophotometry have been implemented for the determination of 4-NP in various environmental samples.[22-26] Among the various detection methods, the electrochemical analytical method shows excellent reliability, sensitivity, selectivity, simple operation, quick response and cost effective. Moreover, most of the research work is focusing on developing higher electrocatalytic activity of electrode materials for the efficient detection of 4-NP by electrochemical analytical methods.

However, there are two major challenges obstructing for wide scale application of environmental remediation and targeted drug delivery. For example, graphene and hydroxyapatite have excellent adsorption capability but it is not easy to separate and recycle after treatment. The magnetite nanoparticles can be able to guide in targeted drug delivery, it have a high recovery ratio, stable performance and it is east to recycle. Therefore, we designed the magnetic electro catalytic systems to be an effective way to resolve the aforementioned problems. Since the magnetic separation technique possesses the advantages of high efficiency, rapidity, and cost-effectiveness. Additionally, tit will effectively eliminate the requirement for either solvent swelling before or catalyst filtration after the reaction.[30]

In the present work, a high energy ball mill can exfoliate the edge-carboxylated graphene (ECG) sheets from natural graphite flakes. Further, the mHAp nanocomposites were dispersed on the prepared two dimensional ECG sheets by using a one pot facile hydrothermal process. The possible synthesis strategies of edge-carboxylated graphene through high energy ball mill and the formation mechanism of m-HAp nanocomposites on the two dimensional ECG sheets are proposed in detail. The glassy carbon electrode modified with this novel m-HAp/ECG nanocomposite exhibits admirable electrocatalytic activity to develop sensitive sensor for the electrochemical detection of 4-NP. The fabricated electrochemical sensor exhibits higher sensitivity, good selectivity and desired lower detection limit.

2. EXPERIMENTAL SECTION

2.1. Materials

Graphite flakes (~105 μm), aspartic acid, di-ammonium hydrogen phosphate ($(NH_4)_2(HPO_4)$), ferrous chloride tetra hydrate ($FeCl_2{\cdot}4H_2O$), ferric chloride hexahydrate ($FeCl_3{\cdot}6H_2O$), 4-nitrophenol and calcium chloride dihydrate ($CaCl_2.2H_2O$) were supplied by Sigma Aldrich. Acetone, hydrochloric acid 5% (HCl) and ethanol were purchased from Himedia Laboratory Pvt. Ltd, India. All these chemicals were of analytical grade and used without further purification.

2.2. Synthesis of edge-carboxylated grephene sheets by high energy ball mill

In a typical process,natural graphite was milled in a planetary ball-mill (Fritsch Pulverisette-P7) in the presence of aspartic acid at 300 rpm for 40 h in a stainless steel vial and ball with the ball to powder weight ratio of 10:1 in air. The obtained product was washed with double distilled water and 5% of HCl solution to remove metal impurities. Further, it was washed with deionized water several times until the pH becomes neutral and dried in vacuum oven at 70°C for 24 h.

2.3 Synthesis of m-HAp on ECG sheets by hydrothermal process

In this process, 50 mg of ECG sheets was suspended in 50 ml of deionized water by ultrasonic dispersion for 30 min to form a stable black colour graphene solution and the supernatant was collected for further process. Further, 30 mM of calcium chloride was dissolved in 30 ml of supernatant graphene solution. Subsequently, 18 mM of di-ammonium hydrogen phosphatewas dissolved in 20 ml of deionized water and gradually added to the above mixture. The pH was adjusted at 10-10.5 by adding ammonium hydroxide solution (30%) and it is represented as solution A. Meanwhile, 5 mM of ferrous chloride and 10 mM of ferric chloride were dissolved in 20 ml of aqueous solution to prepare the 1:1.5 molar ratio of Fe^{2+} and Fe^{3+}. Also, the pH was adjusted to 10-11 by adding ammonium hydroxide solution (30%) to start the nucleation growth of Fe_3O_4 and it is represented as solution B. Subsequently, the solution B was added to solution A with constant stirring for 30 min. Finally, the mixed solution was transferred to the Teflon-lined stainless steel autoclave for hydrothermal treatment. The autoclave was sealed and placed in an oven at 180°C for 12 h and then cooled to room temperature naturally. The obtained precipitate was washed with deionized water and ethanol several times and it was dried in vacuum at 70°C overnight.

2.4. Characterization

X-ray diffraction (XRD) was performed at room temperature using a PANalytical (X-Pert-Pro) diffractometer with Cu

$K\alpha_1$radiation (λ= 1.5406 Å). The average crystallite sizes were estimated using the Scherrer formula. The morphology and elemental analysis of the composite was determined by high resolution transmission electron microscopy (HRTEM) and Field emission scanning electron microscopy (FEI Quanta – 250) with EDX and elemental mapping. The infrared spectrum of the samples was obtained by using a Fourier transform infrared (FTIR) spectrometer (Bruker Tensor 27, Germany). Raman scattering was performed on a JY-1058 Raman spectrometer using a 520 nm laser source. UV-Visible spectral analysis was carried out using JoscoV-650 spectrophotometer. Surface area and pore size distribution of a nanocomposite was determined by using a micromeritics ASAP 2020 surface area analyzer. The X-ray photoelectron spectroscopy (XPS) was carried out on a Kratos Axis Ultra-DLD X-ray photoelectron spectroscope (Manchester, U.K).

2.5 Fabrication of modified glassy carbon electrode using m-HAp/ECG nanocomposite

The m-HAp nanocomposite on ECG was dispersed in ethanol under sonication for 3 h and the resultant solution is hereafter represented as m-HAp/ECG nanocomposite. Meanwhile, the surface of the GCE was carefully mirror polished with alumina slurry followed by washing with double distilled water and ultrasonicated in ethanol containing water for 20 min. Afterwards, *ca.* 8 µL of dispersed m-HAp/ECG (with optimal concentration) was drop cast on the GCE and dried in vacuum at 30 °C. The modified electrode can be represented as m-HAp/ECG modified GCE and it can be exploited for electrochemical detection at room temperature under inert atmosphere.

3. RESULTS AND DISCUSSION

3.1. Structural and morphological characterization m-HAp/ECG

The schematic illustration for the formation of ECG sheets by high energy ball milling of natural graphite flakes in the presence of aspartic acid is shown in Fig . 1 (a). Herein, the planetary ball mill with the speed of 300 RPM can be used to exfoliate the ECG sheets through interaction with aspartic acid under solid condition. The reactive carbon species (carboxylic ions in aspartic acid) and high speed rotation of ball mill produces the cleavage of graphitic C-C bonds at the broken edges. Sufficient kinetic energy is generated during the high energy milling and it compensate the week forces of Van der Waals attraction between two adjacent π-π stacked graphite layers for bond cleavages for the C-C aromatic graphite structure.

The carbon species in aspartic acid react with the selective edges of graphite forming chemically functionalized graphite sheets during the milling process. The aspartic acid could effectively exfoliate graphite with edge-corboxylated species ($-COO^-$) and it protects the re-stacking of graphene layers. The obtained product was suspended in different solvents such as water, ethanol, N, N-dimethylformamide (DMF) and N-methyl-2-pyrrolidone (NMP) under ultra-sonication to remove residual unreacted graphite. These ECG sheets dispersed solution was kept it one week for thorough settling the unreacted graphite. The precipitate was removed and resulting supernatant solutions was kept for 10 days at room temperature to confirm the dispersibility of ECG sheets.The ESI Fig. 1a shows the dispersion of ECG with different solvents of water, ethanol, DMF and NMP for the exfoliating agent of aspartic acid. The as obtained ECG sheets indicate a good stability in DMF and NMP with the concentration of 1 mg/mL.

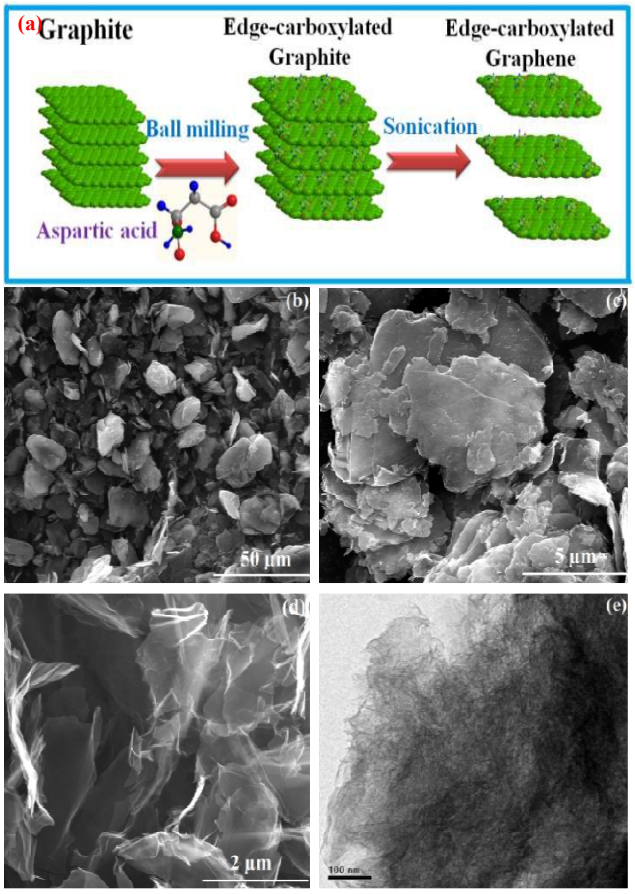

Fig. 1(a) Schematic illustration for the synthesis of ECG sheets by high energy ball milling in the presence of aspartic acid, FESEM image of (a) as-received natural graphite flakes, (c) ECG sheets, (d) exfoliated ECG sheets and (e) TEM images of ECG sheets.

The possible stable highly concentrated dispersion of ECG sheets is due to the electrostatic stabilization and it is further confirmed by Zeta potential analysis. The ESI Fig. 1b shows the Zeta potential of -40.7 mV corresponds to the ECG sheets in water. This reveals the strong repulsive force arises due to the negatively charged carboxylic groups ($-COO^-$) and it was present in the edges of graphene sheets. The morphology of as-received natural graphite flakes shows the larger grain sizes in the range from 80 to 100 µm with flake like morphology as shown in Fig. 1 (b). After 40 h of ball milling in the presence of aspartic acid shows the reduction in the size range of 2-5 µm as seen in Fig. 1(c) due to mechanochemical cleavage of graphite. These ECG sheets were suspended in 10 ml of deionized water under ultrasonic dispersion for 30 min for FESEM and TEM analysis. Fig. 1(d,e) shows the FESEM and TEM images of exfoliated ECG sheets and it reveals the graphene sheets are homogeneously dispersed (2-5 µm) and highly transparent under the electron beam. Figure 3 (a-d) shows the surface morphology and

microstructure of the m-HAp/ECG nanocomposite. Fig.2 (a, b) shows the agglomeration free individual graphene sheets with uniformly distributed m-HAp nanoparticles on the surface as well as edges of the ECG sheets. The high magnification FESEM images in Fig.2(c,d) shows mHAp nanoparticles uniformly dispersed on ECG sheets with an average diameter of 50-100 nm.

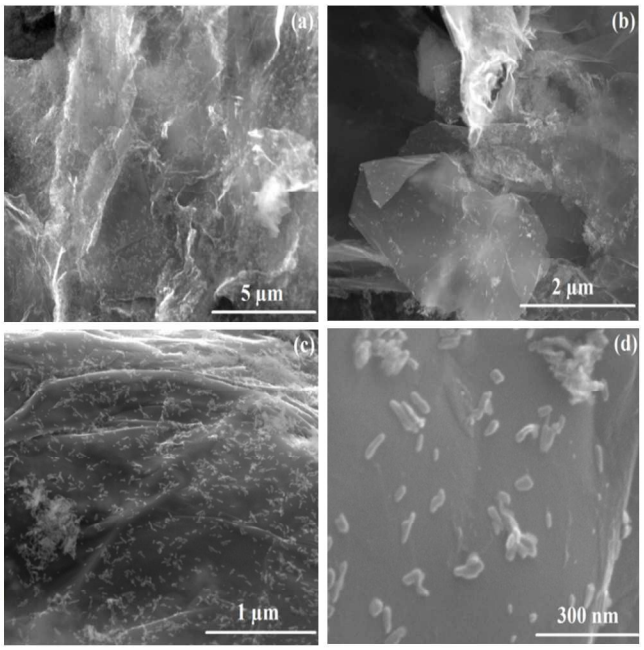

Fig. 2 (a-d) FESEM images of m-HAp/ECG nanocomposite with different magnifications

Schematic representation for the synthesis and possible nucleation growth of m-HAp/ECG nanocomposites is shown in Fig. 3. The edge-carboxylated grapheme sheets are prepared by high energy ball mill in the presence of aspartic acid. The aspartic acid reacts with the selective edges of graphite during the milling and forms a carboxylic (-COO^-) functionalized graphite sheets.

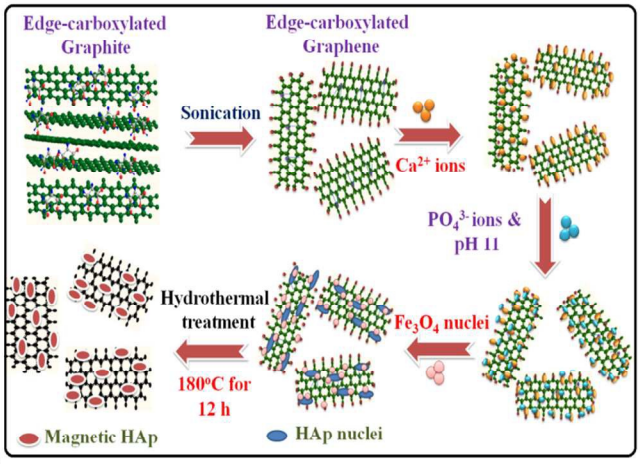

Fig.3 Schamatic represantation for the new strategy for the formation mechanism of m-HAp nanoparticles grown on two dimensional ECG sheets

The number of oxygen containing carbonyl and carboxyl groups was present at the edges, epoxy and hydroxyl group was located at the basal plane of the graphene sheets. These oxygen containing groups were possibly involved the anchoring of m-HAp nanoparticles on the negatively charged ECG sheets. This edge-carboxylated graphite was further exfoliated under ultrasonication for 3 h to make highly stable, block colour suspension in water and the supernatant is collected for further experimental process.

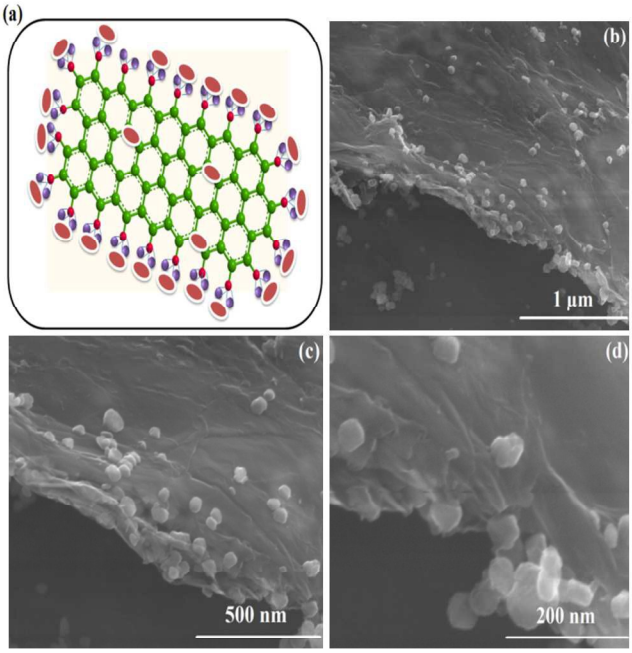

Fig.4 (a) Schamatic illustration for the m-HAp nanoparticles grown on edges of two dimensional ECG sheets and (b-d) FESEM images of m-HAp on ECG sheets with different magnifications.

In brief, 30 mM concentration of $CaCl_2.2H_2O$ was added to the supernatant of ECG solution. The calcium ion (Ca^{2+}) in the solution was selectively bonded with epoxy, hydroxyl and carboxyl group through electrostatic interactions. This Ca^{2+} ion easily diffuses and prefer for the crystallization and growth of HAp nuclei on the edges and basal planes of the ECG sheets. Further, these Ca^{2+} ions react with phosphate (PO_4^{3-}) ions via electrovalent bonds by adjusting the pH. Finally the HAp nuclei were formed on the basal plans and edges of the ECG sheets. Meanwhile, during the nucleation and growth of HAp, certain molar concentration of $Fe^{2+}$and Fe^{3+} (1:2) was added for the preparation of m-HAp nanoparticles on the basal planes and the edges of the ECG sheets which were confirmed through FESEM images. Fig.4 (a,b) shows the morphology of the m-HAp on ECG sheets and it was grown on the edges of graphene sheets due to the presence of -COO^- ions in the graphene sheets. Fig.4 (c, d) shows the uniform dispersion of m-HAp nanocomposite on the edges of graphene sheets with an average diameter of 80 -100 nm. The energy dispersive X-ray (EDX) analysis and elemental mapping as shown in ESI Fig.2 confirms the uniform distribution of carbon (C), oxygen (O), calcium (Ca), phosphorus (P) and iron (Fe) are present in the m-HAp/ECG sheets. It confirms the P, Ca, Fe and O are well dispersed in the m-HAp nanorods and the carbon was well dispersed in the ECG sheets. X-ray powder diffraction (XRD) pattern was used to analyze the crystallinity and phases of the prepared m-HAp/ECG sheets.

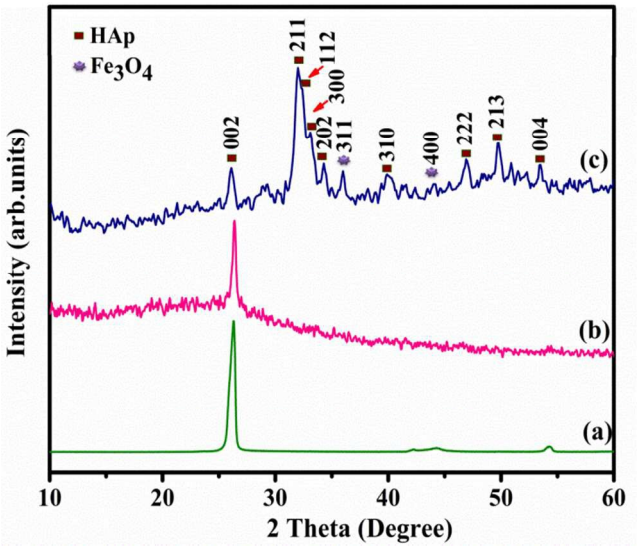

Fig.5 XRD pattern for (a) as-received natural graphite flakes, (b) ball milled edge-carboxylated graphite and (c) m-HAp/ECG nanocomposite.

Fig. 5(a-c) shows the XRD pattern for the pure graphite, ball milled edge-carboxylated graphene and mHAp/ECG sheets. The XRD pattern for the m-HAp/ECG nanocomposite in Fig. 5(c) shows the dual phases of pure HAp (JCPDS #. 09-0432) and Fe_3O_4 (JCPDS #. 89-0688). Fig.5(a) shows a strong diffraction peak at 26.45° for the (002) plane of natural graphite flakes with the *d*-spacing of 0.34 nm. In contrast, the ball milled graphite in the presence of aspartic acid shows the week intense peak at 25.35° for the (002) plane in Fig.5(b) confirms the high degree of carboxyl groups are functionalized in the edges of graphite. It confirms the mechanochemical cleavage of graphitic C-C bonds and also edge-selectively functionalized graphite.

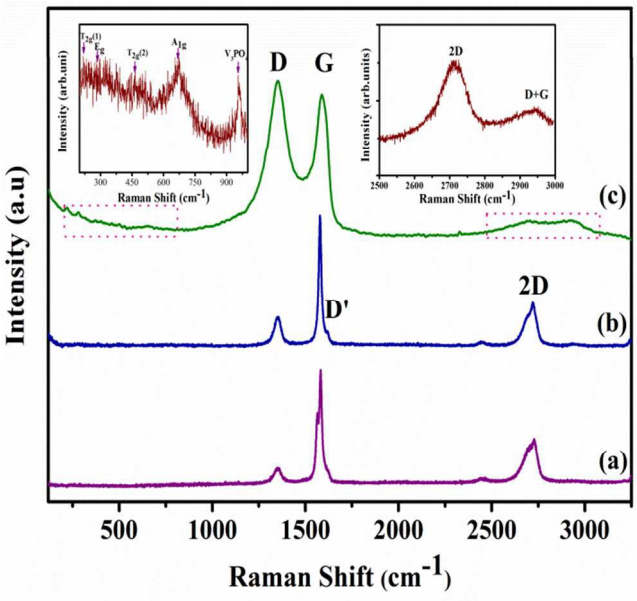

Fig.6 Raman spectra for (a) pure natural graphite flakes, (b) ball milled edge-carboxylated graphene sheets and (c) m-HAp/ECG nanocomposites.

The FTIR spectra for the pure graphite and ball milled ECG samples are shown in ESI Fig. 3 (a-c). The absorption peak at 3443 cm^{-1} is due to the stretching vibration of O-H and 1637 cm^{-1} is attributed to C=C stretching vibration. The FTIR spectrum for the ball milled sample in ESI Fig. 3 (b) shows the peak at 1739 cm^{-1} attributed to the carboxylic group (C=O). The characteristic absorption peaks of methylene groups (CH_2) are observed for the ECG sheets and m-HAp/ECG nanocomposite at 2853 and 2926 cm^{-1} as shown in ESI Fig. 3 (b, c). The intense peaks at 565 and 1039 cm^{-1} are due to bending vibrations and asymmetric stretching vibrations of the O-P-O and P-O in the PO_4^{3-} groups. The additional peak at 600 cm^{-1} is attributed to the lattice absorption of iron oxide (Fe-O). Therefore, FTIR results confirm the carboxylic group could be introduced at the broken edges of graphite during the ball milling and the m-HAp nanoparticles are successfully grown on edges of ECG sheets.The Raman spectra in Fig. 6 completes the structural analysis of pure graphite, ball milled edge-carboxylated graphene and m-HAp/ECG nanocomposite. Fig.6(a) shows the Raman spectrum for the pure graphite with two prominent peaks at 1580 and 2970 cm^{-1} corresponds to the well documented G and 2D bands respectively. The weak D band at 1346 cm^{-1} was associated for the vibration of A_{1g} symmetry of sp^3 carbon atoms and correlated to defect ordered structural peak. It is well-known that the G and 2D band corresponds to the first-order scattering of the E_{2g} phonon of carbon sp^2 atoms and second-order double resonant process with opposite momentum in the highest optical branch near the K points in the Brillouin zone (Bz) of graphene. The calculated intensity ratio of D to G (I_D/I_G) is approximately 0.02 for the pure natural graphite flakes. In contrast, the Raman spectrum for the ball milled edge-carboxylated graphene in Fig. 6(b) shows a strong D band at 1331cm^{-1}. The intensity ratio of D and G band (I_D/I_G) is 0.5 suggests the significant edge functionalization in the presence of aspartic acid. Fig.6(c) shows the Raman spectrum for the m-HAp/ECG nanocomposite.

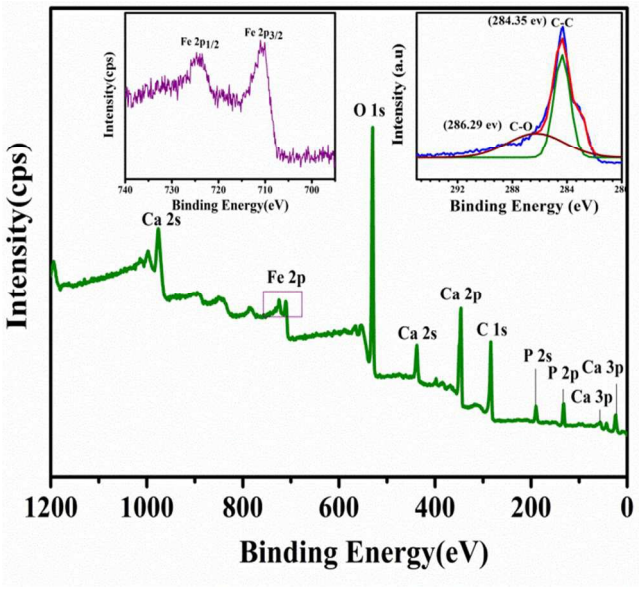

Fig.7 The XPS wide scan spectrum of mHAp/ECG nanocomposite with left and right inset figure is a high resolution spectrum of C1s and Fe2p.

The right insert in Fig. 6(c) shows the magnetite phase of the composite and the peak at 669 cm^{-1} can be ascribed to the

magnetite A_{1g} active mode and less intense peaks at 540 and 309 cm^{-1} corresponds to the Raman active modes of T_{2g} and E_g for magnetite. In addition the characteristic band at 960 cm^{-1} assigned to the symmetric stretching (ν_1) of the phosphate group (PO_4^{3-}).The optical absorption of ECG sheets and m-HAp/ECG nanocompsites are studied by UV-vis spectroscopy with the initial concentration of 0.1 mg/ml in water. Two prominent absorption peaks were observed at 230 and 300 nm for the ECG sheets as shown in ESI Fig. 4 (a). The peak at 230 nm is due to the π- π* plasmon peak for the nanoscale sp^2 C=C aromatic transition bonds. Further the broader peak at 300 nm was attributed to n-π* transition peak of sp^3 C=O bonds. It suggests the edges of graphite were highly carboxylated during the planetary mill with the presence of aspartic acid. The characteristic peak of ECG is red shifted from 230 to 255 nm may be due to the hydrothermal reduction reaction between ECG sheets and mHAp as shown in ESI Fig. 4 (b). The phase and elemental composition of the as-prepared m-HAp/ECG nanocomposite was further analysed using XPS. Fig.7 shows the wide scan XPS spectrum for the m-HAp/ECG nanocomposite exhibits photoelectron lines at binding energies of 347.07, 133.13, 284, 530 and 711 eV corresponds to Ca 2p, P 2p, C 1s, O 1s and Fe 2p, respectively. The right inset high-resolution C1s XPS spectrum of the mHAp/ECG nanocomposite shows a sharp intense peak at 284.35 eV corresponds to sp^2 aromatic structure of C-C bonds in a conjugated honeycomb lattice. The intense peak at 286.29 eV is attributed to the C-O bonding due to harsh oxidation of graphene sheets by the mechanochemical synthesis in the presence of aspartic acid. The high-resolution Fe 2p XPS spectrum is placed in left corner of Fig.7 and the binding energies at 711.2 and 724.8 eV are associated to Fe $2p_{3/2}$ and Fe $2p_{1/2}$ respectively. This result clearly confirms the Fe_3O_4 and HAp phases are well dispersed on the mechanochemically synthesized ECG sheets through hydrothermal process.

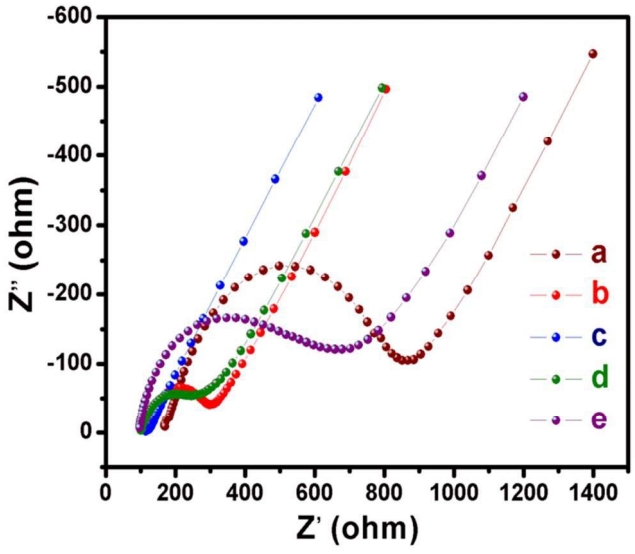

Fig.8 EIS plots of 5.0 mM $[Fe(CN)6]^{3-/4-}$ in 0.1 M KCl recorded at different electrodes of Pure graphene (a), Pure Hap (b), m-HAp/ECG (c), m-HAp (d) and bare (e) modified GCE.

The surface area and pore size distribution of the m-HAp/ECG nanocomposite was further determined from nitrogen physisorption (adsorption-desorption) measurements. The ESI Fig. 5 shows the adsorption-desorption isotherm and corresponding pore size distribution. The isotherm shows a type IV loop at a relative pressure between 0 to1. The specific surface area and pore size distribution for the m-HAP/ECG nanocomposite using Barrett-Joyner-Halenda (BJH) calculation are 130 m^2g^{-1} and 5 -20 nm respectively. The magnetic properties of the nanocomposites have been investigated at room temperature using a vibrating sample magnetometer (VSM) with an applied magnetic field of ±2 KOe. The ESI Fig. 6 shows the magnetic hysteresis loop for the mHAp/ECG nanocomposite. The obtained saturation magnetization (M_s) and coercivity (Hc) are 11.12 emu/g and 0.12 Oe respectively.

In order to analyze the electrochemical sensing mechanism, resistance, diffusion coefficient, and charge transfer resistance at the electrode/electrolyte interfaces, the electrochemical impedance spectroscopy (EIS) study is performed. As we known, the diameter of the semicircle is a direct representation of the charge transfer resistance (Rct). Fig.8 depicts the Nyquist plots of pure graphene (a), pure HAp (b), m-HAp/ECG (c), m-HAp (d) and bare (e) modified GCE, studied in 5 mM $Fe(CN)_6^{3-/4-}$ and 0.1 M KCl used as the supporting electrolyte. Fig.8 shows that the pure graphene and bare GCE has higher R_{ct} when compared with the other three modified electrodes, and the R_{ct} values of other modified GECs have decreased effectively. Hence, the m-HAp/ECG modified GCE exhibits the lowest Rct value than the other modified electrodes, which suggest the m-HAp/ECG as optimized electrode for electrochemical analysis based on the obtained lower R_{ct} value.

3.2. Electrochemical detection of 4-Nitrophenol by modified GCE with m-HAp/ECG nanocomposite

The electrocatalytic performance of the m-HAp/ECG nanocomposite was studied by modifying the GCE with this nanocomposite using cyclic voltammograms (CV). Fig.9 shows the cyclic voltammogram curves of 200µM 4-NP in 0.05 M acetate buffer solution with a pH of 5.0 at various electrodes such as bare GCE, m-HAp and m-HAp/ECG nanocomposite. There was no signal observed at the modified GCE without 4-NP. The addition of 4-NP in bare GCE shows not much difference in the CV curve with a weak peak current at E_{pc} (cathodic peak potential). Further, a noticeable signal observed at 0.77 V for the pure HAp, pure graphene, and m-HAp nanocomposite modified GCE. The well-defined redox peak and significant cathodic peak potential (E_{pc}) and anodic peak potential (E_{pa}) were observed at -0.77 and 0.21 V for the mHAp/ECG nanocomposite modified GCE. Fascinatingly, m-HAp/ECG-modified GCE exhibits a remarkable sharp peak at 0.76 V with enhanced peak current, as shown in ESI Fig. 7.It concludes the electrochemical detection of 4-NP is a reversible two electron transfer reduction-reduction process.[31-33] Subsequently, the molecular structure and the electron transfer mechanism can be explained in scheme 1.

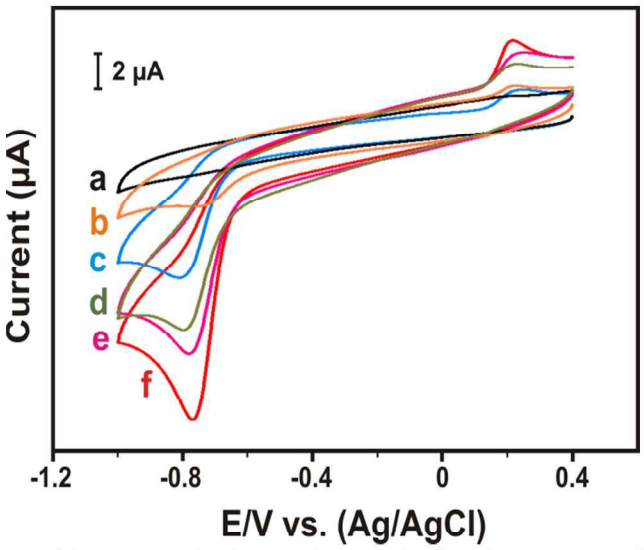

Fig.9 (a) CV curve in the absence of 4-NP in the electrolyte. CV curves of (b) bare GCE, (c) pure HAp, (d) pure graphene (e) m-HAp and (f) m-HAp/ECG nanocomposite modified GCE in the presence of 200µM 4-NP in 0.05 M acetate buffer solution with the pH of 5.0 at 50 mVs^{-1}.

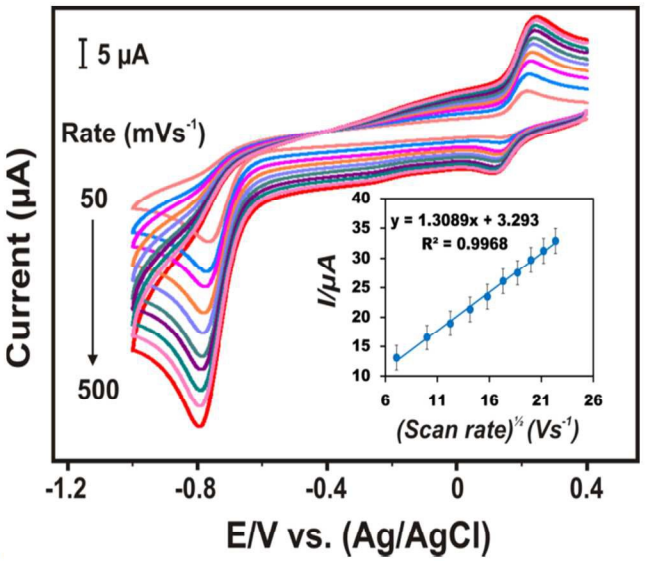

Fig. 10 CV curves of m-HAp/ECG-modified GCE in the presence of 200 µM 4-NP in 0.05 M acetate buffer solution with pH 5.0 recorded at different scan rates from 50 to 500 mVs^{-1}. Inset: correlations between peak currents and square root of scan rate.

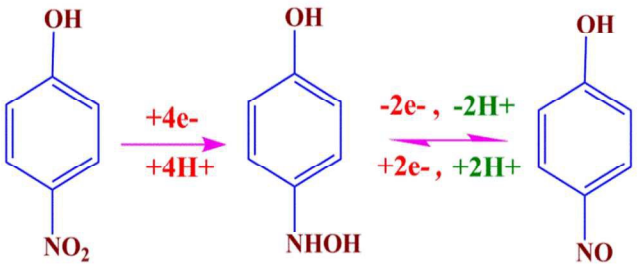

Scheme 1. Molecular structures and electrochemical detection mechanism of 4-Nitrophenol

Accordingly, a redox peaks occur at a peak potential at -0.77 and 0.25 V due to $4e^-/4H^+$ reduction of the nitro group of the hydroxylamine species. This suggests the 4-NP molecules could be adsorbed by the various modified electrodes and are reduced at -0.77 V. The CV curves clearly confirms the m-HAp/ECG nanocomposite modified GCE exhibits the best electrochemical detection of 4-NP. The obtained cathode peak current also higher than the already reported values for the sensing of 4-NP with modified electrodes.[24-32] This should be due to the increase in the specific surface area and adsorption sites that increases the current response for the sensing of 4-NP in m-HAp/ECG nanocomposites. The influence of scan rate on electrochemical activity of m-HAp/ECG nanocomposite modified GCE also studied by measuring the CV with different scan rates of 50 to 500 mVs^{-1}. Fig. 10 shows the CV curves with different scan rates of m-HAp/ECG modified GCE for 4-NP detection. It shows the reduction peak current increases with the increase of scan rate in the range from 50 to 500 mVs^{-1}. Moreover, a linear increase occurs between the redox peak current and the square root of the scan rate as expected for typical diffusion-controlled process. For better under understanding, we provide a correlation plot for E_0 *vs* peak currents in ESI Fig. 7. These results confirm the observed CV responses are due to the detection of 4-NP molecules diffused on the surface of m-HAp/ECG nanocomposite modified GCE.

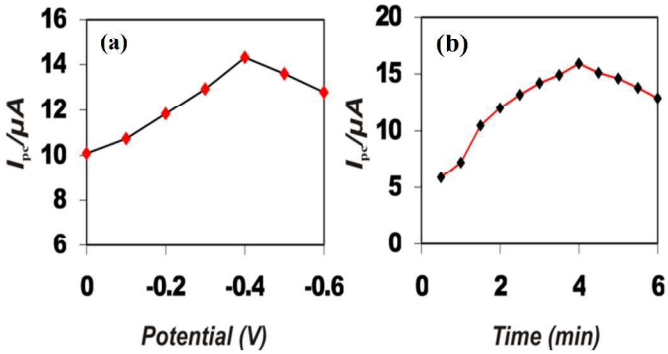

Fig. 11 Variations of peak current with (a) accumulation potential and (b) time during the detection of 200µM of 4-NP.

The inset in Fig.10 shows the plot between reduction peak current and the square root of scan rate which may be expressed by a linear regression equation as $E_{pa}(V) = 1.3089x + 3.293$, R^2=0.9968. All these results clearly confirm the process is diffusion controlled reversible process.[31] Fig. 11 (a, b) shows the influence of accumulation potential and time on the electrochemical activity of the m-HAp/ECG nanocomposite modified GCE explored by DPV measurements. The peak current increases with the accumulation potential in the range from 0 to -0.4 V. This indicates the amount of adoptive accumulation of 4-NP on the surface of m-HAp/ECG nanocomposites modified GCE. The adoptive accumulation of 4-NP reaches surface saturation at -0.6 V by further increasing the accumulation potential as shown in Fig. 11 (a). The Fig.11 (b) shows the effect of accumulation time on the detection of 4-NP and a maximum peak current was observed at the accumulated time of 4 min. Therefore, the accumulation potential of -0.4V and time of 4 min are chosen to achieve the optimal condition for the detection of 4-NP.

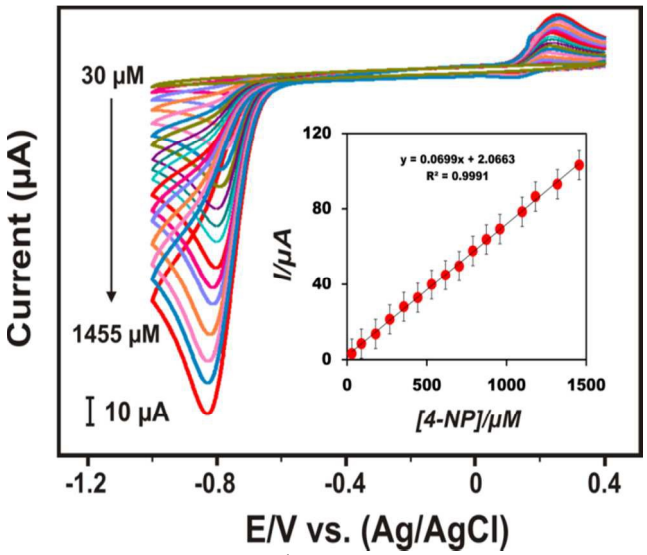

Fig. 12 CV curves of m-HAp/ECGmodified GCE under various 4-NP concentrations of 30-1455 μM at 50 mVs^{-1}. Inset; cathodic reduction peak current (I_{pc}) *vs* 4-NP concentration.

The analytical performance of the 4-NP sensor was compared by studying the electrocatalytic performance by using both CV and DPV. Fig. 12 shows the cyclic voltammogram curves for the detection of 4-NP with different concentrations of 4-NP in the range from 30-1455 μM in acetate buffer solution with pH 5. The peak current is increasing with the increasing concentration of 4-NP. The insert in Fig. 12 corresponds to the electrochemical analytical curve shows the linear dependence of peak current (I_{pc}) with the various 4-NP concentrations. Further, the potential shift of the peak currents is not affected much by their increasing 4-NP concentration as shown in ESI Fig. 9. The detection limit (LOD) can be calculated by using the following equation.

$$LOD = \frac{3S_b}{b} \quad (1)$$

The LOD can be calculated from the standard deviation of the mean value for ten voltammograms of the blank (S_b) and the slope of the straight line of the electrochemical analytical curve. The attributed analytical parameters of 4-NP are more comparable with the various modified electrodes summarized in Table 1. The differential pulse voltammetry (DPV) studies can be employed to obtain the sensitivity of the fabricated 4-NP sensor. Fig. 13 shows the DPV responses of the 4-NP reduction at different concentrations with the optimal experimental conditions. Fig. 13 shows the DPV response of the m-HAp/ECG modified GCE for the detection of 4-NP with different concentrations of 0.2-994 μM in the presence of 0.05 M acetate buffer solution with pH 5.

Table 1 Comparison of analytical parameters for the detection of 4-NP with various modified electrodes

Electrode substrate	Detection limit (μM)	Concentration range (μM)	Sensitivity ($\mu A \mu M^{-1} cm^{-2}$)	Reference
mHAp/ECG[a]/GCE[b]	0.27	0.2-994	0.587±0.002	Present work
AC[c]	0.16	1-500	5.810±0.24	26
Graphene/Nf[d]/SPCE[e]	0.6	10-620	---	36
Au NPs[f]/GCE	8.0	10-1,000	---	37
Ag particles/GCE	0.5	1.5-140	0.043	38
Nano-Cu_2O/GCE	0.5	1-400	---	39
HA-NP[g]/GCE	0.6	1-300	---	40

[a]ECG- Edge-carboxylated graphene; [b]GCE – glassy carbon electrode; [c]AC – activated carbon [d]Nf – nafion; [e]SPCE – screen printed carbon electrode; [g]HA-NP – hydroxyapatite nano powder.

Also, there is no saturation response observed for the concentration of 994 μM and the sensitivity has calculated from the slope of the calibration plot as shown in the inset of Fig 13. The calculated sensitivity is 0.587342 (±0.002) $\mu A \mu M^{-1} cm^2$. The calculated lower detection limit (LOD) was 0.27 μM acc. to the formula of LOD=3 sb/S (where s_b is the standard deviation of the blank signal, and S is the sensitivity). The calculated detection limit of 0.27 μM is lower than those required for environmental control by the United States (US) EPA in the occasion of drinking water (0.43 μM). Besides, corresponding DPV curves at anodic peak current (I_{pa}) also observed with the various concentrations between 23-472 μM. Fig. 13 shows, the catalytic activity of the 4-NP increases with increasing concentration of 4-NP and a linear regression values and correlation coefficient as $I_{pa}(V) = 0.0068x + 0.2278$ and R^2=0.9791 respectively. The detection limit was 2.5 μM observed from the slope of the calibration plot as shown in the insert in Fig.13. These results indicate the catalytic performance of cathodic reduction is higher than the anodic oxidation. Moreover, the cathodic reduction is more favorable for the detection of 4-NP to avoid the interference arises from foreign species (particularly ascorbic acid) in real time applications.[32] Obviously, the m-HAp/ECG modified GCE exhibits much higher sensitivity and lower detection limit of 4-NP with higher concentrations compared to other reports (see

Table 1).

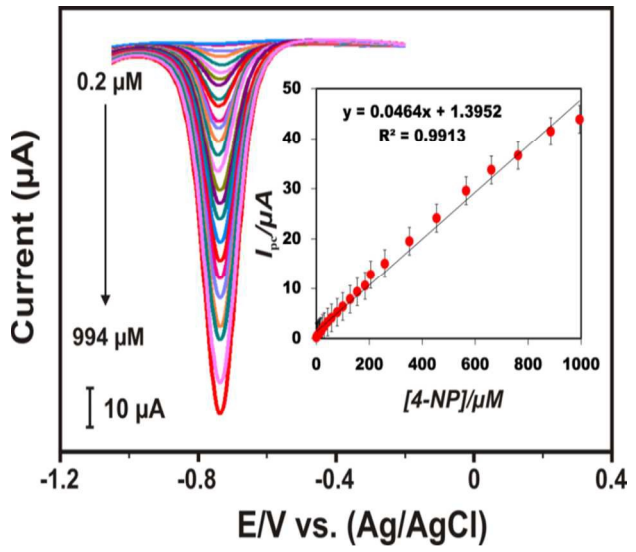

Fig. 13 DPV curves of m-HAp/ECG modified GCE for various 4-NP concentrations of 0.2-994 μM. Inset- cathodic reduction peak current (I_{pc}) *vs* 4-NP concentration.

Stability, reliability and real sample analysis

The stability of the reported 4-NP sensor was examined by using DPV measurements using m-HAp/ECG modified GCE by measuring the cathodic peak current periodically. The sensor retains 91.36% of its initial reduction peak current response after 20 days at room temperature reveals the good storage stability. In addition, a separate DPV measurement also carried out for the 3 different m-HAp/ECG modified GCE prepared under the same conditions, which shows an acceptable reproducibility with relative standard deviation (RSD) of 3.2%. Moreover, the repeatability for 5 successive measurements with the RSD of 2.16% for the determination of 200 μM 4-NP suggests a good repeatability of the sensor.

Real sample analysis

The m-HAp/ECG modified GCE was further explored to detect the 4-NP in tap and rain water for the real sample analysis. DPV was adopted to estimate the accuracy of the detection of 4-NP from these real samples. The obtained results are given in Table S1 and it confirms the good electrochemical responses of both tap and rain water. The obtained recovery values ranges from 97.4 and 105.9%, which reveals the appreciable practicality of the 4-NP sensor.

4. Conclusion

In summary**,** we have established a simple possible approach to produce the mass production of ECG sheets with the assistance of aspartic acid by eco-friendly ball milling process under solid condition. The obtained ECG sheets was highly dispersible in various solvents like water, ethanol, DMF and NMP. The ECG sheets show a good stability of dispersion in water with a Zeta potential of -40 mV. Further, the m-HAp nanoparticles were uniformly grown on the edges and basal plane of ECG sheets using hydrothermal process with an average diameter of 80-100 nm. Anovel 4-nitrophenol detection with superior electrocatalytic performances was obtained by modifying the GCE with the prepared m-HAp/ECG nanocomposite. The electrocatalytic performance of the 4-NP sensor was evaluated by cyclic voltammogram (CV) and differential pulsed voltammetry (DPV). The fabricated sensor exhibits an excellent electrocatalytic performance with a low detection limit and high sensitivity of 0.27 μM and 0.587 μA $\mu M^{-1}cm^{-2}$ respectively.

AUTHORS INFORMATION

[a]*Department of Nanoscience and Technology, Bharathiar University, Coimbatore 641 046, India.*
[b]*Electroanalysis and Bioelectrochemistry Lab, Department of Chemical Engineering and Biotechnology, National Taipei University of Technology, Taiwan.*
[c]*Defence Metallurgical Research Laboratory, Kanchanbaugh, Hyderabad 500 058, India.*
**Corresponding author, E-mail:ponpandian@buc.edu.in*

Acknowledgements

The authors would like to acknowledge the University Grant Commission (UGC), Government of India, and New Delhi for the financial support and DST – PURSE, Government of India for FESEM facility.

References

1 K. S. Novoselov, V. I. Fal'ko, L. Colombo, P. R. Gellert, M. G. Schwab and K. A. Kim, *Nature*. 2012, **490**, 192–200.
2 V. Leo´n, A. M. Rodriguez, P. Prieto, M. Prato, and E. Va´zquez. *ACS Nano*. 2014, **8**, 563-571.
3 D. Wei, B. Wu, Y. Guo, G. Yu and Y. Liu, *Acc. Chem. Res*.2013, **46**, 106-115.
4 E. Pallecchi, F. Lafont, V. Cavaliere, F. Schopfer, D. Mailly, W. Poirier and A. Ouerghi. *Sci. Rep*. 2014, **4**, doi:10.1038/srep04558.
5 G. S. Shmavonyan, G.G. Sevoyan, V. M. Aroutiounian., *Am. J. Phys*, 2013, 6, 1-6.
6 T. Lin, J. Chen, H. Bi, D. Wan, F. Huang, X. Xiaoming and M.Jiang. *J. Mater. Chem. A*, 2013, **1**, 500-504.
7 W. W. Liu and J. N. Wang. *Chem. Commun*., 2011, **47**, 6888-6890.
8 D.V. Kosynkin, A. L. Higginbotham, A. Sinitskii, J. R. Lomeda, A. Dimiev, B. K. Price and J. M. Tou. *Nature*, 2009, **458**, 872-876.
9 W. S. Hummers, and R.E. Offeman. *J. Am. Chem. Soc*. 1958, **80**, 1339.
10 D. C. Marcano, D. V. Kosynkin, J. M. Berlin, A. Sinitskii, Z. Sun, A. Slesarev, L. B. Alemany, W. Lu, and J. M. Tour. *ACS Nano*. 2010, **4**, 4806-4814.
11 V. Leo´n, M. Quintana, M. A. Herrero, J. L. G. Fierro, A. Hoz, M. P. E. Va´zquez. *Chem. Commun*. 2011, **47**, 10936-10938.
12 M. Jong Ju, In-Yup Jeon, K. Lim, J. C.Kim, H. J. Choi, I. T. Choi, Y. K. Eom, Y. J. Kwon, J. Ko, J. Joon Lee, J. Beom Baek and H. Kyu Kim., *Energy Environ. Sci*., 2014,*7*, 1044-1052.
13 Y. Jeon, Y. R. Shin, G. J. Sohn, H. J. Choi, S. Y. Bae, J. Mahmood, S. M. Jung, J. M. Seo, M. J. Kim, D. W. Chang, L. Dai, and J. B. Baek. *PNAS*. 2012, ***109***, 5588-5593.
14 Y. Jeon, H. J. Choi, M. Choi, J. M. Seo, S. M. Jung, M. J. Kim, S. Zhang, L. Zhang, Z. Xia, L. Dai, N. Park and J. B. Baek. *Sci. Rep*. 2013, **3: 1810**, 1-7.
15 V. V. Singh, G. Gupta, A. Batra, A. K. Nigam, M. Boopathi, P. K. Gutch, B. K. Tripathi, A. Srivastava, M. Samuel, G. S. Agarwal, B. Singh and R. Vijayaraghavan,. *Adv. Funct. Mater*. 2012, **22**, 2352-2362.
16 V. V. Singh, A. K. Nigam, S. S. Yadav, B. K. Tripathi, A. Srivastava, M. Boopathi and B. Singh., *Sens. Actuators, B*., 2013,***188***, 1218-1224

17 Y.T. Kong, M. Boopathi andY. B. Shim, *Biosens. Bioelectron*. 2003, ***19***, 227-232.

18 C. Fu, W. Yang, X. Chen and D. G. Evans, *Electrochem. Commun*. 2009, **11**, 997-1000.

19 Y. Guo, Y. Han, S. Shuang and C. Dong., *J. Mater. Chem*., 2012, **22**, 13166-13173.

20 M. R. Na, W. Bin, L. Yan, L. Jing, Z. Qian, W. G. Tao, J. W. Li and W. H. Sheng., *Sci China Ser B-Chem*. 2009 ,**52 (11)**, 2013-2019.

21 L. Junhua, D. Kuang, Y. Feng, F. Zhang and M. Liu., *Microchim Acta,* 2012,**176**, 73-80.

22 L. Junhua, D. Kuang, Y. Feng, F. Zhang, Z. Xu, M. Liu. J. Hazard. Mater., 2012, 201, 250-259.

23 J. Liu, Y. Chen, Y. Guo, F. Yang, and F. Cheng, Journal of Nanomaterials. 2013, 2013, 1-6. doi:10.1155/2013/632809.

24 Y. Zeng, Y. Zhou, T. Zhou and G. Shi., *Electrochimica Acta*. 2014, **130**, 504-511.

25 X. Kong, Z. Sun, M. Chen, C. Chen and Q. Chen. *Energy Environ. Sci*., 2013, **6**, 3260-3266.

26 R. Madhu, C. Karuppiah, S. M. Chen, P. Veerakumar and S. B. Liu. *Anal. Methods,* 2014, **6** , 5274-5280

27 Y. P. Guo, T. Long, S. Tang, Y. J. Guo and Z. A. Zhu. *J. Mater. Chem. B*, 2014, **2**, 2899-2909.

28 E. B. Ansar, M. Ajeesh, Y. Yokogawa, W. Wunderlich and H. Varma. *J. Am. Ceram. Soc*., 2012, **95**, 2695-2699.

29 M. Iafisco, M. Sandri, S. Panseri, J. D. Pez, A. G. Morales and A. Tampieri. *Chem. Mater.* 2013, **25**, 2610-2617.

30 Y. Qiu, Z. Ma and P. An Hu, *J. Mater. Chem. A*, 2014, **2**, 13471-13478.

31 L. Luo, X. Zou, Y. Ding and Q.Wu. *Sens. Actuators, B*, 2008, **135**, 61-65.

32 F. C. Moraes, S. T. Tanimoto, G. R. S. Banda, S. A. S. Machado, L. H. Mascaro. *Electroanalysis*, 2009, **21**, 1091- 1098.

33 M. A. Mhammedi, M. Achak, M. Bakasse and A. Chtaini. J. Hazard. Mater. 2009, 163, 323-328.

34 C. K. Honeychurch, J. P. Hart. *Electroanalysis*, 2007, **19**, 2176 - 2184.

35 G. S. Garbellini, G. R. S. Banda, L.A. Avaca. *Food Chem*. . 2009, 116, 1029-1035.

36 A. Arvinte, M. Mahosenaho, M. Pinteala, A. M. Sesay, V. Virtanen,*Microchim. Acta*, 2011, **174**, 337.

37 L. Chu, L. Han and X. Zhang, *J. Appl. Electrochem.*, 2011, **41**, 687.

38 I. G. Casella and M. Contursi, *J. Electrochem.Soc.,* 2007, **154**, 697.

39 H. Yin, Y. Zhou, S. Ai, Q. Ma, L. Zhu and L. Lu, *Inter. J. Environ. Anal. Chem.,* 2012, **92**, 742.

40 H. Yin, Y. Zhou, S. Ai, X. Liu, L. Zhu and L. Lu, *Microchemi. Acta,* 2010, **169,** 87.